Journal of Materials Chemistry A

LiF-doped sulfide solid electrolytes with a stabilized α-Li3PS4 analog phase for all-solid-state Li metal batteries

Journal:	*Journal of Materials Chemistry A*
Manuscript ID	TA-ART-09-2024-006831.R1
Article Type:	Paper
Date Submitted by the Author:	30-Nov-2024
Complete List of Authors:	Asakura, Taichi; Osaka Metropolitan University, Department of Applied Chemistry Izawa, Ryo; Osaka Metropolitan University Kimura, Takuya; Osaka Metropolitan University, Department of Applied Chemistry Hotehama, Chie; Osaka Metropolitan University, Department of Applied Chemistry Kowada, Hiroe; Osaka Metropolitan University Deguchi, Minako; Osaka Metropolitan University Motohashi, Kota; Osaka Metropolitan University, Department of Applied Chemistry Sakuda, Atsushi; Osaka Metropolitan University, Department of Applied Chemistry Tatsumisago, Masahiro; Osaka Metropolitan University, Department of Applied Chemistry Hayashi, Akitoshi; Osaka Metropolitan University - Nakamozu Campus, Department of Applied Chemistry

ARTICLE

LiF-doped sulfide solid electrolytes with a stabilized α-Li_3PS_4 analog phase for all-solid-state Li metal batteries

Received 00th January 20xx,
Accepted 00th January 20xx

DOI: 10.1039/x0xx00000x

Taichi Asakura, Ryo Izawa, Takuya Kimura, Chie Hotehama, Hiroe Kowada, Minako Deguchi, Kota Motohashi, Atsushi Sakuda, Masahiro Tatsumisago, and Akitoshi Hayashi*

All-solid-state Li metal batteries require solid electrolytes with both high reduction tolerance and high Li-ion conductivity. Adding LiF, which has a wide potential window, to these solid electrolytes effectively improves their reduction tolerance. However, this addition decreases the conductivity of the solid electrolyte. In this study, we subjected LiF-doped Li_3PS_4 glass to a heat-treatment process involving rapid heating and quenching. This process precipitated a highly ionic conductive α-Li_3PS_4 analog phase, thereby achieving both high conductivity and high reduction tolerance. The Li_3PS_4·LiF glass-ceramic electrolyte with the precipitated α-Li_3PS_4 analog phase exhibited a high conductivity of 1.3×10^{-3} S cm^{-1} at room temperature. Galvanostatic cycling tests of Li symmetric cells and SEM observations of the Li/solid electrolyte interface indicated that the Li_3PS_4·LiF glass-ceramic electrolyte showed compatibility with Li metal. Therefore, Li_3PS_4·LiF glass-ceramic electrolyte successfully combines the high conductivity of the α-Li_3PS_4 analog phase with the excellent electrochemical stability of LiF. This work proposes a new approach to developing solid electrolytes for all-solid-state Li metal batteries.

Introduction

All-solid-state batteries are considered promising next-generation energy storage devices because of their higher energy density and improved safety performance (non-flammability and no liquid leakage) compared to conventional Li-ion batteries.[1–3] Sulfide electrolytes are characterized by good formability[4] and high conductivity,[5–9] making them attractive materials as solid electrolytes in all-solid-state batteries.

Li_3PS_4, a well-known sulfide electrolyte, exhibits several crystal polymorphs[5,10–12] with different conductivities. Its thermodynamically stable crystalline phase, γ-Li_3PS_4, exhibits a low conductivity of 10^{-7} S cm^{-1} at room temperature.[10] Moreover, β-Li_3PS_4, a middle-temperature phase, has an ionic conductivity of approximately 10^{-4} S cm^{-1} at room temperature.[11] The thermodynamically nonequilibrium phase, Li_3PS_4 glass, has a conductivity above 10^{-4} S cm^{-1} at room temperature.[5] Recently, the crystal structure of the high-temperature phase, α-Li_3PS_4, was reported[12] and its high conductivity was predicted.[13–15] In our previous study, we revealed that α-Li_3PS_4 can be stabilized at room temperature by rapidly heating Li_3PS_4 glass to crystallize it, followed by quenching.[16] The ionic conductivity of the glass-ceramic sample with precipitated α-Li_3PS_4 was 1.3×10^{-3} S cm^{-1} at room temperature, which is an order of magnitude higher than that of the β-phase and glass. Among the crystal polymorphs of Li_3PS_4, the α-phase has the highest conductivity. Therefore, it is expected to be applied in all-solid-state batteries.

To develop all-solid-state batteries with high energy density, the application of Li metal negative electrodes is desired because of their high theoretical capacity (3860 mA h g^{-1}) and lowest redox potential (−3.04 V vs. SHE).[17,18] However, the practical implementation of Li metal negative electrodes is prevented by short circuits due to Li dendrite (filament) formation[19–22] To investigate the cause of the short circuit, our research group has focused on the chemo-mechanical behavior at the interface between Li metal and Li_3PS_4. The contact of Li_3PS_4 with Li metal forms a decomposition layer at the interface because of Li_3PS_4 reduction.[23–26] This decomposition layer is mainly composed of Li_2S and Li_3P.[23] The volume expansion due to the decomposition forms microcracks in the reduction layer.[25] The Li filaments then propagate along the microcracks, react with Li_3PS_4 at reaction fronts, and form a further reduction layer.[25] As described above, the formation of the decomposition layer and the growth of Li filaments are repeated and sometimes lead to large cracks, resulting in short circuits.

Various strategies have been explored to suppress the growth of Li filaments and to inhibit reductive decomposition. Such strategies include the insertion of a metallic intermediate layer at the interface[26–28] and the addition of lithium halide, which is thermodynamically stable to Li, to the solid electrolyte.[24,29–32] These approaches have improved short-circuit tolerance by suppressing the direct contact between Li metal and Li_3PS_4 and

Department of Applied Chemistry, Graduate School of Engineering, Osaka Metropolitan University, 1-1 Gakuen-cho, Naka-ku, Sakai, Osaka 599-8531, Japan.
E-mail: akitoshihayashi@omu.ac.jp
Supplementary Information available: [details of any supplementary information available should be included here]. See DOI: 10.1039/x0xx00000x

increasing the reduction tolerance of the solid electrolyte, respectively. Lithium fluoride (LiF) inhibits the growth of Li filaments owing to its wide potential window[33] and low electronic conductivity. However, as LiF is a poor ionic conductor, its addition decreases the ionic conductivity of the solid electrolyte and increases the overall cell resistance.[34,35] Even in solid electrolytes with high reduction tolerance, higher conductivity allows the Li metal negative electrode to operate at higher current densities without short-circuiting.[31] Therefore, the development of highly conductive LiF-doped solid electrolytes may realize stable cycling of all-solid-state Li metal batteries at higher current densities.

In this study, LiF-doped Li_3PS_4 glasses were mechanochemically prepared, and LiF-doped Li_3PS_4 glass-ceramic samples were prepared via a heat treatment involving rapid heating and rapid cooling. Systematic characterization of the Li_3PS_4–LiF glasses and glass-ceramic samples was performed by investigating their chemical structure, electrochemical properties, and Li metal compatibility using all-solid-state Li symmetric cells. The fabricated solid electrolytes were also applied to an all-solid-state Li/S battery and evaluated using discharging-charging tests.

Experimental

Materials Synthesis

All syntheses were carried out in a dry argon-filled glovebox. $Li_3PS_4{\cdot}x$LiF (molar ratio, x = 0., 0.1, 0.2, 0.5, 1.0) glasses were obtained using a mechanochemical process. Li_2S (99.9%; Mitsuwa Chemicals Co., Ltd.), P_2S_5 (99%; Sigma-Aldrich Co., LLC), and LiF (99%; Stella Chemifa Corp.) were used as starting materials. All starting materials (3 g) were ball-milled in a 250 mL ZrO_2 pot with 450 g of 4 mm ϕ ZrO_2 balls in a planetary ball mill (PULVERISETTE 5; Fritsch GmbH).

$Li_3PS_4{\cdot}x$LiF (molar ratio) glass-ceramic samples were prepared by a rapid heating and quenching process based on our previous report.[16] The glass powder was wrapped in Al foils and sandwiched between the two preheated hot plates for 1 min. The Al foil containing the sample was then removed and quenched by pressing it down with a metal plate at room temperature to obtain a glass-ceramic sample. The temperatures of the preheated hot plate and metal plate were set in the range of 195–392 °C, as measured by a thermocouple. During this treatment, the heating rate was approximately 400 °C min^{-1} or higher.

Characterization

To examine the sample structures, X-ray diffraction (XRD) measurements (SmartLab; Rigaku Corp.) were performed using Cu Kα radiation. The 2θ angle range and scan speed were 10°–60° and 5° min^{-1}, respectively.

X-ray photoelectron spectroscopy (XPS, K-alpha; Thermo Fisher Scientific) was performed to reveal the chemical bonding of the samples. The samples were transferred to the XPS instrument in a dry Ar gas atmosphere. Monochromatic Al-Kα radiation (1486.6 eV) was used as the X-ray source. To compensate for surface charging effects, the samples were neutralized during the measurement using a flood gun. Subsequently, the samples were etched using an Ar^+ ion monomer.

The local structures of the samples were investigated using Raman spectroscopy with a Raman spectrometer (LabRAM HR-800; HORIBA, Ltd.). The measurements were conducted in a dry Ar atmosphere, and the light source was an yttrium aluminum garnet laser (λ = 532 nm).

^{31}P magic-angle-spinning nuclear magnetic resonance (^{31}P MAS NMR) experiments were performed using an NMR spectrometer (JNM-ECX 400; JEOL Ltd.). The sample powders were packed into zirconia spinners under a dry Ar atmosphere. The observation frequency was 161.8 MHz. NMR spectra were collected using a π/2 pulse length of 3.5 μs and a recycle delay of 10 s while rotating at 12 kHz. Chemical shifts were externally referenced to ammonium dihydrogen phosphate ($NH_4{\cdot}H_2PO_4$).

The thermal behavior of the glass powders was analyzed using differential thermal analysis (DTA, Thermo Plus TG8110; Rigaku Corp.). The glass powders were sealed in Al pans in a dry Ar atmosphere. The heating rate was 10 °C min^{-1}.

The ionic conductivities of the prepared samples were determined using an impedance analyzer (SI-1260, Solartron Analytical). The sample powders were pelletized using a uniaxial press at 360 MPa for 5 min at room temperature. Both sides of the pellets were then coated with Au thin films as an ion-blocking electrode using a quick coater (Quick Coater SC-701; Sanyu Electron Co., Ltd). Each powder compact was vacuum-sealed in an aluminum-laminated pouch cell. Alternating current (AC) impedance measurements were performed by applying an AC voltage of 10 mV in the frequency range of 0.1 Hz to 10 MHz.

Evaluation of all-solid-state cells

All-solid-state cells were fabricated in a dry argon-filled glovebox. All-solid-state Li symmetric cells were assembled in polycarbonate dies (10 mm ϕ). The solid electrolytes (150 mg) were pelletized by uniaxial pressing at 360 MPa, and Li foil (99.9%, 250 μm; Furuuchi Chemical Corp.) was attached to both sides of the pellet. Based on our previous report, the cell stack pressure was set at 5 MPa after once applying a pressure of 16 MPa.[36] The maximum current density at which the cell could operate without short-circuiting was used as a measure of Li stripping/plating performance. For the Li symmetric cells, a current density was applied for 1 h per half cycle. The current density was increased every five cycles at intervals of 0.064 mA cm^{-2}. Galvanostatic cycling tests were performed at a constant current density of 0.1 mA cm^{-2}, with the amount of Li metal to be stripped and plated at 0.1 mA h cm^{-2} per half cycle. These electrochemical measurements were conducted at room temperature (26 ± 3 °C) using an electrochemical workstation (Celltest 1470E; Solartron Analytical). The morphology of the Li/solid electrolyte interface after cycling was observed using

scanning electron microscopy (SEM, SU8220; Hitachi, Ltd.) to evaluate the stability of the solid electrolyte to Li metal. In case the solid electrolyte layer was very fragile, a focused ion beam (FIB)-SEM instrument (JIB 4700F; JEOL Ltd.) was used to observe the Li/solid electrolyte interface.

An all-solid-state Li/S cell was fabricated as follows. A sulfur–carbon (S–C) composite was prepared using a previously reported method.[37] Then, the S–C composite and $54Li_3PS_4 \cdot 46LiI$ (mol %) glass (LPSI) were mixed to obtain the S–C–LPSI composite positive electrode.[36] The weight ratio of sulfur in this composite was 40 wt%. The composite positive electrode (1.8 mg) and the solid electrolyte (100 mg) were pelletized by uniaxial pressing at 360 MPa in a polycarbonate cylinder. Li metal foil was used for the negative electrode. Stainless steel rods were used as current collectors for both electrodes. The stack pressure of the cells was also set to 5 MPa after once applying a pressure of 16 MPa. Charge–discharge tests of the fabricated Li/S cell were performed in an electrochemical workstation (VMP3; BioLogic Science Instruments) at a current density of 0.10 mA cm^{-2} (1/10 C) at room temperature in an Ar atmosphere.

Results and discussion

Fig. 1a shows the XRD patterns of $Li_3PS_4 \cdot x$LiF samples prepared by the mechanochemical process, where x represents the molar ratio. Halo patterns were mainly observed for all samples, indicating that they were in the glass state. Peaks attributed to LiF appeared for samples with $x \geq 0.2$, indicating that LiF is partially present in the crystalline state. XPS was performed to investigate the bonding states within $Li_3PS_4 \cdot x$LiF glasses. The F 1s XPS spectra are displayed in Fig. 1b. The glass with $x = 0.1$ showed a different bonding state for F at 684 eV (green line) compared to LiF at 685 eV (blue line). This suggests that LiF is partially incorporated into the Li_3PS_4 glass matrix. The peak intensity of LiF increased with increasing LiF content, primarily because of the limit of LiF dissolution into the Li_3PS_4 glass. These results were also confirmed by the F KLL spectra obtained by XPS (Fig. S1). Fig. 1c shows the DTA curves of the milled samples. Exothermic peaks corresponding to the crystallization of β-Li_3PS_4 were observed between 200–300°C. These peaks shifted to lower temperatures as the amount of LiF added increased. This observation also indicates that LiF was incorporated into the Li_3PS_4 glass. The glasses were characterized by Raman spectroscopy, and bands attributed to PS_4^{3-} and $P_2S_6^{4-}$ units were observed (Fig. S2). The addition of LiF did not significantly change the amorphous structure of Li_3PS_4.

$Li_3PS_4 \cdot x$LiF glass-ceramic samples were prepared by heat treating the LiF-doped Li_3PS_4 glasses. The glasses were heated to targeted temperatures with a rapid heating rate of 400 °C min^{-1}, followed by quenching. The crystal polymorph of Li_3PS_4 in the prepared glass-ceramic sample was identified by analyzing the number of characteristic peaks within the 2θ range of 17−19°, similar to previous reports.[12,38] Specifically, the high-temperature phase, α-Li_3PS_4, showed one peak, and the medium-temperature phase, β-Li_3PS_4, displayed two peaks. Fig. 2a shows the XRD patterns of $Li_3PS_4 \cdot 0.5$LiF glass-ceramic samples at room temperature, prepared by heat treatments at various target temperatures from 195 °C to 299 °C. The sample heat-treated at 195 °C exhibited a halo pattern and LiF peaks. The sample heat-treated at 214 °C showed a pattern similar to that of β-Li_3PS_4. When the heat-treatment temperature was further increased, a pattern similar to that of α-Li_3PS_4 was observed, and β-Li_3PS_4 was precipitated again when the sample was annealed at 281 °C or higher. Thus, the α-Li_3PS_4 analog was stabilized at room temperature in the LiF-doped Li_3PS_4 glass-ceramic samples. This trend in the XRD patterns from amorphous, to β-Li_3PS_4 analog phase, to α-Li_3PS_4 analog phase, and back to the β-Li_3PS_4 analog phase with increasing target temperature of the heat treatment was also observed for Li_3PS_4 without LiF addition.[16] No change was observed in the LiF peaks regardless of the target heat-treatment temperatures. The composition dependence of the crystal polymorphs of the glass-ceramic samples obtained by rapidly heating and quenching $Li_3PS_4 \cdot x$LiF glasses at various target temperatures is summarized in Fig. 2b. While the high-temperature α-phase was obtained for Li_3PS_4 over a wide temperature range,[16] the temperature range in which the α-Li_3PS_4 analog phase was obtained became narrower when a small amount of LiF was added. As the amount of LiF added increased, the range of heat treatment temperature at which the α-Li_3PS_4 analog precipitated became larger. This would have occurred because the increase in LiF content in the sample inhibits the arrangement of PS_4 units during crystallization, forming a high-temperature phase that more closely resembles the structure of the melt. The effect of LiF addition on the lattice parameter was investigated by intensity decomposition of XRD patterns of Li_3PS_4 and $Li_3PS_4 \cdot$LiF glass-ceramic samples. The fitting was performed based on the structures of β-Li_3PS_4 and LiF. The results are shown in Tables S1 and S2. No significant change in lattice parameter and volume was observed with the addition of LiF. Fig. 2c shows the F 1s XPS spectra of the $Li_3PS_4 \cdot x$LiF glass-ceramic samples containing the α-Li_3PS_4 analog. Compared to the glass samples, the amount of incorporated F in the glass-ceramics samples was reduced, and the intensity of the LiF peak was stronger. This tendency was also confirmed by the F KLL spectra in Fig. S3. This is because some F in the glass precipitated as LiF during crystallization, increasing the relative proportion of LiF in the samples. To obtain more detailed information, $Li_3PS_4 \cdot$LiF glass and glass-ceramic samples were evaluated using ^{19}F MAS-NMR measurements (Fig. S4). In the ^{19}F MAS-NMR spectrum of the glass sample, in addition to a peak at −205 ppm attributed to LiF, a peak was observed at approximately −182 ppm, which may be attributed to the F incorporated in the glass matrix. In the NMR spectrum of the glass-ceramic sample, a peak corresponding to LiF was mainly observed, suggesting that F precipitated as LiF from the amorphous matrix upon crystallization. In addition, PS_4^{3-} units were observed in the glass-ceramic samples using ^{31}P MAS-NMR and Raman spectroscopy (Fig. S5 and S6).

Next, the conductivities of the $Li_3PS_4 \cdot x$LiF glass and glass-ceramic samples on which the α-Li_3PS_4 analog phase was

precipitated were evaluated using AC impedance measurements. The dependence of sample composition on conductivity at room temperature and activation energy is shown in Fig. 3. The temperature dependence of the conductivity of all samples obeyed the Arrhenius law. The conductivity of Li_3PS_4·*x*LiF glasses decreased with the addition of LiF. This decrease was caused by the presence of a large amount of LiF with low ionic conductivity in the samples. Li_3PS_4·*x*LiF glass-ceramic electrolytes with the precipitated α-Li_3PS_4 analog phase showed improved conductivity compared to the Li_3PS_4·*x*LiF glasses. The conductivity of the Li_3PS_4·0.1LiF glass-ceramic electrolyte was lower than that of the glass-ceramic electrolyte without LiF. This would have occurred because a certain amount of the β-phase co-precipitated, probably due to the narrow range of the target temperature of the α-Li_3PS_4 analog phase precipitation when a small amount of LiF was added. By increasing the amount of LiF, the conductivity of the samples exceeded 10^{-3} S cm^{-1}, with a maximum of 1.3×10^{-3} S cm^{-1} at x = 1. Notably, these values represent high conductivities even for solid electrolytes containing large amounts of LiF. These high conductivities are attributed to the addition of LiF, which facilitated the stabilization of the α-Li_3PS_4 analog phase at room temperature. This phase was responsible for the major ionic conduction in the samples. LiF crystallized from glasses would be uniformly dispersed in α-Li_3PS_4 glass-ceramics, and the close contact between LiF and the α-Li_3PS_4 /glass phase is thought to reduce grain-boundary resistance and maintain high conductivity of α-Li_3PS_4 glass-ceramics. In addition, the activation energies of LiF-doped Li_3PS_4 after heat treatment were significantly lower than those before the heat treatment. This can also be explained by the stabilization of the highly ionic conducting α-Li_3PS_4 analog phase at room temperature.

To investigate the compatibility of the prepared solid electrolytes with Li metal, Li stripping/plating performance was evaluated using the Li symmetric cells. Cycling tests were performed to investigate the maximum current density of the cells without short-circuiting. The current density was set to increase by 0.064 mA cm^{-2} for every five cycles, and the Li metal was stripped and plated for 1 h in each cycle at room temperature. As shown in Fig. 4a, the Li symmetric cell with the Li_3PS_4 glass-ceramic electrolyte failed after the current density increased above 0.13 mA cm^{-2}. In contrast, the cell with the Li_3PS_4·LiF glass-ceramic electrolyte operated without short-circuiting even at a current density of 0.57 mA cm^{-2}. Considering that these solid electrolytes have comparable conductivities of 10^{-3} S cm^{-1}, it is clear that the addition of LiF enhanced the Li stripping/plating performance. In addition, Li symmetric cells with the Li_3PS_4·LiF glass, whose conductivity was reduced by adding LiF, showed no significant improvement in Li stripping/plating performance (Fig. S7). Therefore, both high conductivity and high reduction tolerance are crucial for developing a solid electrolyte with high short-circuit tolerance. The galvanostatic cycling test of the Li symmetric cell with the Li_3PS_4·LiF glass-ceramic electrolyte (Fig. 4b) also demonstrated stable operation at 0.1 mA cm^{-2} for more than 500 h without overpotential increase. We observed that the Li_3PS_4·LiF glass-ceramic electrolyte exhibited high stability against Li metal. Furthermore, cross-sectional SEM images of the Li/solid electrolyte interface were obtained after cycling the Li symmetric cells. The cell with the Li_3PS_4 glass-ceramic electrolyte was too fragile after Li stripping and plating. Therefore, FIB milling was performed near the interface before SEM. The backscattered SEM images in Fig. 4c show an intermediate contrast interphase at the Li/Li_3PS_4 interface, which was approximately 75 μm thick. The interphase layer, represented by the different contrasts, is the reaction layer formed via the reductive decomposition of Li_3PS_4. We previously reported that this reduction layer causes the volume of Li_3PS_4 to expand, thereby forming small cracks that cause short circuits. [25] In this experiment, the short circuit is thought to have occurred in the early stages of cycling by the same mechanism. Fig. 4d shows the cross-sectional SEM image of the Li/Li_3PS_4·LiF glass-ceramic electrolyte interface using the backscattered electron detector. A thin reduction layer of approximately 1 μm was observed at the interface, indicating that the addition of LiF significantly suppressed the reductive decomposition. This is based on the low electronic conductivity of the reduction layer by LiF at the Li/solid electrolyte interface. We reported that Li_3PS_4 decomposed reductively at the interface between Li metal and Li_3PS_4, forming a reaction layer composed of Li_3PS_4, Li_2S and Li_3P.[23] Since Li_3P is an mixed conductor, the reaction layer has both Li-ion and electron conductivities. Therefore, the reaction front proceeded continuously to the electrolyte separator, and the reaction layer became thicker when Li_3PS_4 was used. In this study, the electronic conductivity of the reduction layer was decreased by adding LiF, which has low electronic conductivity, resulting in a kinetically stable interface. The short-circuit suppression effect of LiF addition is also investigated in terms of densification of the glass-ceramic electrolytes. The relative densities of the pelletized Li_3PS_4 and Li_3PS_4·LiF glass-ceramics were 84.5% and 81.2%, respectively. Since the addition of LiF tends to rather decrease the relative density, no improvement in Li dendrite suppression by LiF doping is expected in terms of pellet density. Thus, LiF-doping is effective in chemical reduction stability to Li metal, leading to maintaining good interface after cycling test. Hence, we developed a Li_3PS_4·LiF glass-ceramic electrolyte with excellent short-circuit tolerance, which is attributed to the reduction tolerance of LiF-doping and high conductivity of the α-Li_3PS_4 analog.

Finally, the Li_3PS_4·LiF glass-ceramic electrolyte was used as a solid electrolyte in the all-solid-state Li/S battery. Fig. 5 shows the charge–discharge curves and cycling performance of the fabricated all-solid-state Li/S battery. The Li/Li_3PS_4·LiF glass-ceramics/S–C–LPSI cell operated without short-circuiting for 100 cycles, demonstrating the stable operation of the all-solid-state Li/S battery. Discharge plateaus corresponding to the reduction reaction of sulfur were observed at approximately 2 V, and relatively high capacities of approximately 1200 mA h g^{-1} per weight of sulfur were obtained. The charge capacity was somewhat larger than the discharge capacity in the first cycle,

likely due to the involvement of a part of the $54Li_3PS_4 \cdot 46LiI$ glass in the composite positive electrode in the charge-discharge process. At the 100th cycle, 87% of the maximum discharge capacity was maintained. The decreased capacity is probably due to less stack pressure during cycling. The stack pressure optimized for Li metal negative electrode was applied in this study, but it may be insufficient to suppress the volume change of the sulfur positive electrode. Such stable operation and relatively high reversibility of the all-solid-state Li/S battery are ascribed to the high conductivity and high reduction tolerance of the $Li_3PS_4 \cdot LiF$ glass-ceramic electrolyte, which provides low resistance and suppresses overvoltage rise. Therefore, the $Li_3PS_4 \cdot LiF$ glass-ceramic electrolyte is a suitable solid electrolyte for Li metal negative electrode utilization.

Conclusions

Li_3PS_4–LiF glass-ceramic electrolytes were prepared. The α-Li_3PS_4 analog phase was successfully stabilized at room temperature via crystallization with rapid heating and quenching of the LiF-doped Li_3PS_4 glasses. As the amount of LiF added increased, the target temperature range of the heat treatment where the α-Li_3PS_4 analog phase precipitated became wider. Although the conductivity of $Li_3PS_4 \cdot x$LiF glasses decreased with the addition of LiF, it increased by heat treatment with rapid heating and quenching. The conductivity of the $Li_3PS_4 \cdot LiF$ glass-ceramic electrolyte was 1.3×10^{-3} S cm^{-1}, which is 10 times higher than that of the glass electrolyte. The compatibility of the $Li_3PS_4 \cdot LiF$ glass-ceramic electrolyte with Li metal was evaluated using a Li symmetric cell. The addition of LiF suppressed the reductive decomposition of the solid electrolyte and improved Li stripping/plating performance. The $Li_3PS_4 \cdot LiF$ glass-ceramic electrolyte was also applied in all-solid-state Li/S batteries and demonstrated stable operation, confirming its compatibility with Li metal negative electrodes. Overall, we found that the high reduction tolerance and high conductivity of the solid electrolyte significantly contribute to the feasible utilization of Li metal negative electrodes in all-solid-state batteries.

Author contributions

TA: conceptualization, methodology, formal analysis, data curation, investigation, writing – original draft, writing – review & editing. RI, TK and CH: conceptualization, methodology, formal analysis, data curation, investigation. HK and MD: formal analysis, data curation, investigation. KM: supervision, writing – review & editing. AS: conceptualization, methodology, supervision, writing – review & editing. MT: supervision, resources, writing – review & editing, funding acquisition. AH: conceptualization, methodology, supervision, resources, writing – review & editing, funding acquisition.

Conflicts of interest

There are no conflicts to declare.

Data availability

The data are available from the corresponding author on reasonable request.

Acknowledgments

This work was financially supported by the Japan Science and Technology Agency ALCA-SPRING and GteX projects (grant numbers JPMJAL1301 and JPMJGX23S5).

Notes and references

1 C. Sun, J. Liu, Y. Gong, D. P. Wilkinson and J. Zhang, *Nano Energy*, 2017, **33**, 363–386.
2 A. Manthiram, X. Yu. and S. Wang, *Nat. Rev. Mater.*, 2017, **2**, 1–16.
3 K. H. Park, Q. Bai, D. H. Kim, D. Y. Oh, Y. Zhu, Y. Mo and Y. S. Jung, *Adv. Energy Mater.*, 2018, **8**, 1–24.
4 A. Sakuda, A. Hayashi and M. Tatsumisago, *Sci. Rep.*, 2013, **3**, 2261.
5 A. Hayashi, S. Hama, H. Morimoto, M. Tatsumisago and T. Minami, *J. Am. Ceram. Soc.*, 2004, **84**, 477–479.
6 H. Yamane, M. Shibata, Y. Shimane, T. Junke, Y. Seino, S. Adams, K. Minami, A. Hayashi and M. Tatsumisago, *Solid State Ionics*, 2007, **178**, 1163–1167.
7 N. Kamaya, K. Homma, Y. Yamakawa, M. Hirayama, R. Kanno, M. Yonemura, T. Kamiyama, Y. Kato, S. Hama, K. Kawamoto and A. Mitsui, *Nat. Mater.*, 2011, **10**, 682–686.
8 Y. Kato, S. Hori, T. Saito, K. Suzuki, M. Hirayama, A. Mitsui, M. Yonemura, H. Iba and R. Kanno, *Nat. Energy*, 2016, **1**, 1–7.
9 Y. Li, S. Song, H. Kim, K. Nomoto, H. Kim, X. Sun, S. Hori, K. Suzuki, N. Matsui, M. Hirayama, T. Mizoguchi, T. Saito, T. Kamiyama and R. Kanno, *Science*, 2023, **381**, 50–53.
10 M. Tachez, J. P. Malugani, R. Mercier and G. Robert, *Solid State Ionics*, 1984, **14**, 181–185.
11 Z. Liu, W. Fu, E. A. Payzant, X. Yu, Z. Wu, N. J. Dudney, J. Kiggans, K. Hong, A. J. Rondinone and C. Liang, *J. Am. Chem. Soc.*, 2013, **135**, 975–978.
12 K. Homma, M. Yonemura, M. Nagao, M. Hirayama and R. Kanno, *J. Phys. Soc. Jpn*, 2010, **79** Supplement A, 90–93.
13 J. S. Kim, W. D. Jung, S. Choi, J. W. Son, B. K. Kim, J. H. Lee and H. Kim, *J. Phys. Chem. Lett.*, 2018, **9**, 5592–5597.
14 K. Kaup, L. Zhou, A. Huq and L. F. Nazar, *J. Mater. Chem. A*, 2020, **8**, 12446–12456.
15 F. N. Forrester, J. A. Quirk, T. Famprikis and J. A. Dawson, *Chem. Mater.*, 2022, **34**, 10561–10571.
16 T. Kimura, T. Inaoka, R. Izawa, T. Nakano, C. Hotehama, A. Sakuda, M. Tatsumisago and A. Hayashi, *J. Am. Chem. Soc.*, 2023, **145**, 14466–14474.
17 J. M. Tarascon and M. Armand, *Nature*, 2001, **414**, 359–367.
18 D. Lin, Y. Liu and Y. Cui, *Nat. Nanotechnol.*, 2017, **12**, 194–206.
19 M. Nagao, A. Hayashi and M. Tatsumisago, *Electrochem. Commun.*, 2012, **22**, 177–180.
20 J. Kasemchainan, S. Zekoll, D. S. Spencer Jolly, Z. Ning, G. O. Hartley, J. Marrow and P. G. Bruce, *Nat. Mater.*, 2019, **18**, 1105–1111.
21 L. Porz, T. Swamy, B. W. Sheldon, D. Rettenwander, T. Frömling, H. L. Thaman, S. Berendts, R. Uecker, W. C. Carter and Y. M. Chiang, *Adv. Energy Mater.*, 2017, **7**, 1701003.

22 E. Kazyak, R. Garcia-Mendez, W. S. LePage, A. Sharafi, A. L. Davis, A. J. Sanchez, K.-H. Chen, C. Haslam, J. Sakamoto and N. P. Dasgupta, *Matter*, 2020, **2**, 1025–1048.
23 A. Kato, H. Kowada, M. Deguchi, C. Hotehama, A. Hayashi and M. Tatsumisago, *Solid State Ionics*, 2018, **322**, 1–4.
24 M. Suyama, A. Kato, A. Sakuda, A. Hayashi and M. Tatsumisago, *Electrochim. Acta*, 2018, **286**, 158–162.
25 M. Otoyama, M. Suyama, C. Hotehama, H. Kowada, Y. Takeda, K. Ito, A. Sakuda, M. Tatsumisago and A. Hayashi, *ACS Appl. Mater. Interfaces*, 2021, **13**, 5000–5007.
26 T. Inaoka, T. Asakura, M. Otoyama, K. Motohashi, A. Sakuda, M. Tatsumisago and A. Hayashi, *J. Phys. Chem. C*, 2023, **127**, 10453–10458.
27 A. Kato, M. Suyama, C. Hotehama, H. Kowada, A. Sakuda, A. Hayashi and M. Tatsumisago, *J. Electrochem. Soc.*, 2018, **165**, A1950–A1954.
28 H. Wan, Z. Wang, W. Zhang, X. He and C. Wang, *Nature*, 2023, **623**, 739–744.
29 E. Rangasamy, Z. Liu, M. Gobet, K. Pilar, G. Sahu, W. Zhou, H. Wu, S. Greenbaum and C. Liang, *J. Am. Chem. Soc.*, 2015, **137**, 1384–1387.
30 H. Zhang, X. Li, S. Hao, X. Zhang and J. Lin, *Electrochim. Acta*, 2019, **325**, 134943.
31 M. Takahashi, T. Watanabe, K. Yamamoto, K. Ohara, A. Sakuda, T. Kimura, S. Yang, K. Nakanishi, T. Uchiyama, M. Kimura, A. Hayashi, M. Tatsumisago and Y. Uchimoto, *Chem. Mater.*, 2021, **33**, 4907–4914.
32 S. Yang, M. Takahashi, K. Yamamoto, K. Ohara, T. Watanabe, T. Uchiyama, T. Takami, A. Sakuda, A. Hayashi, M. Tatsumisago and Y. Uchimoto, *Solid State Ionics*, 2022, **377**, 115869.
33 W. D. Richards, L. J. Miara, Y. Wang, J. C. Kim and G. Ceder, *Chem. Mater.*, 2016, **28**, 266–273.
34 S. Ujiie, T. Inagaki, A. Hayashi and M. Tatsumisago, *Solid State Ionics*, 2014, **263**, 57–61.
35 F. Zhao, Q. Sun, C. Yu, S. Zhang, K. Adair, S. Wang, Y. Liu, Y. Zhao, J. Liang, C. Wang, X. Li, X. Li, W. Xia, R. Li, H. Huang, L. Zhang, S. Zhao, S. Lu and X. Sun, *ACS Energy Lett.*, 2020, **5**, 1035–1043.
36 T. Asakura, T. Inaoka, C. Hotehama, H. Kowada, K. Motohashi, A. Sakuda, M. Tatsumisago and A. Hayashi, *ACS Appl. Mater. Interfaces*, 2023, **15**, 31403–31408.
37 A. Sakuda, Y. Sato, A. Hayashi and M. Tatsumisago, *Energy Technol.*, 2019, **7**, 1900077.
38 K. Homma, M. Yonemura, T. Kobayashi, M. Nagao, M. Hirayama and R. Kanno, *Solid State Ionics*, 2011, **182**, 53–58.

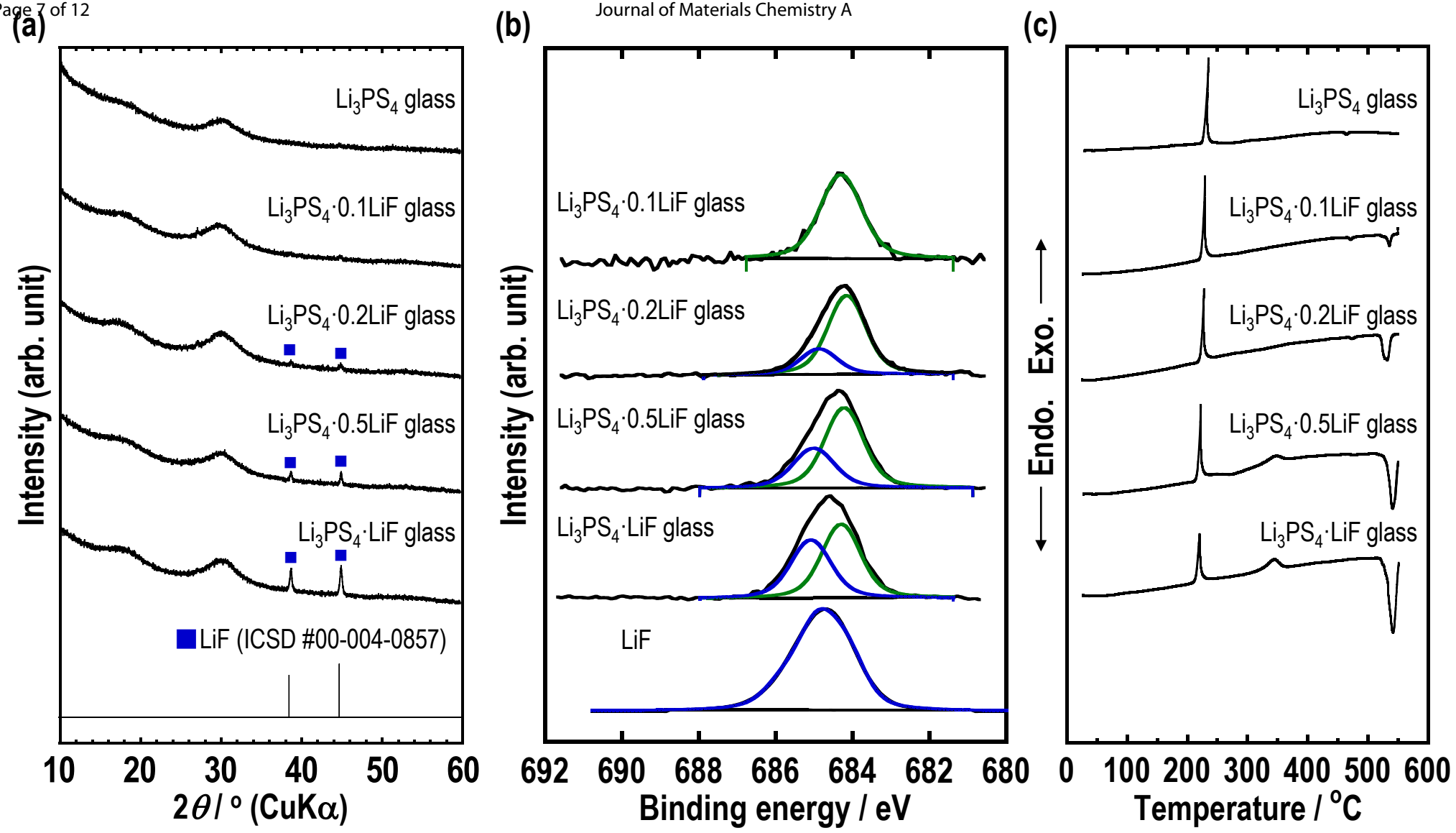

Figure 1 (a) XRD patterns, (b) F 1s XPS spectra, and (c) DTA curves of the $Li_3PS_4 \cdot xLiF$ glasses.

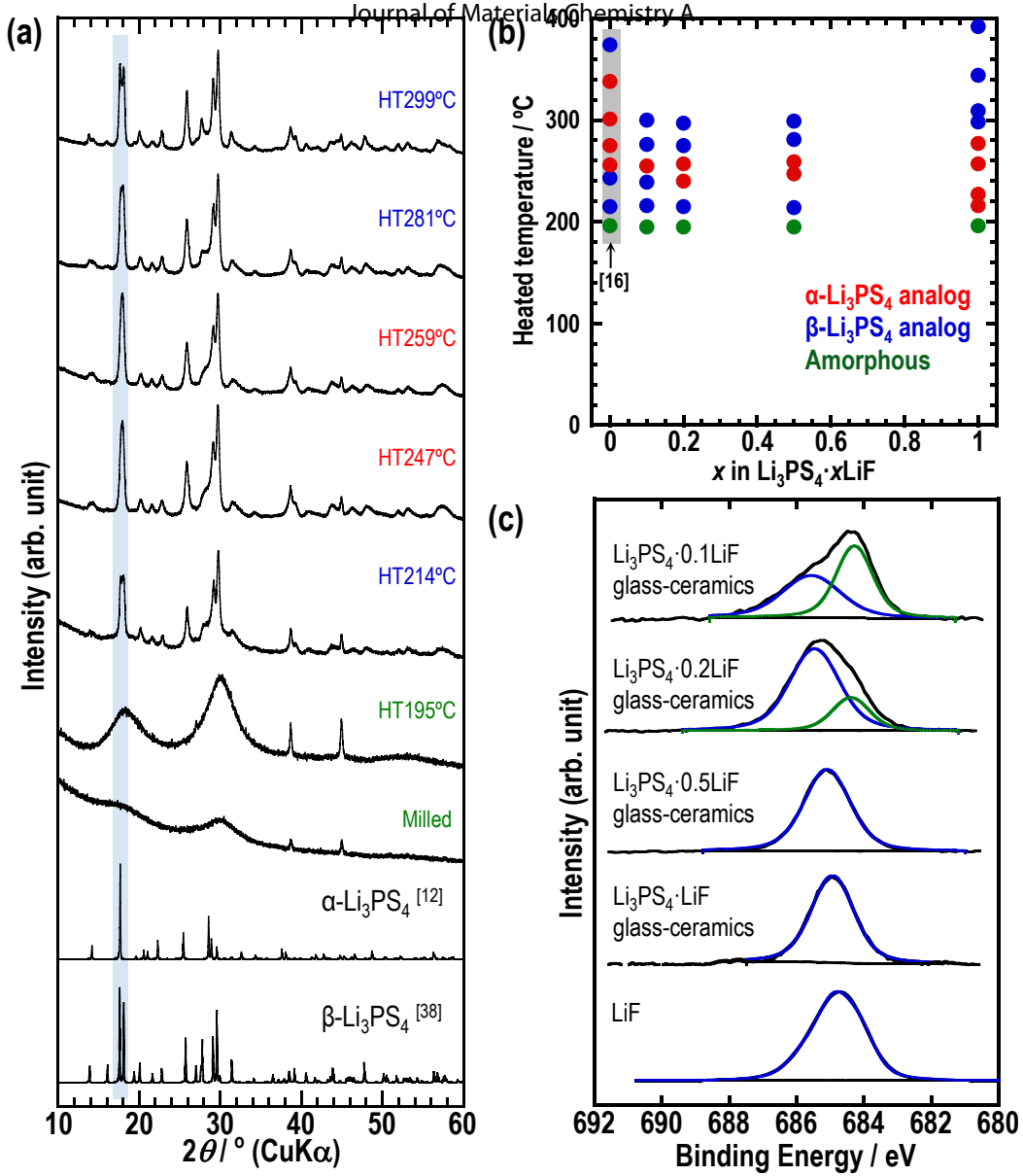

Figure 2 (a) XRD patterns of the Li_3PS_4·0.5LiF glass-ceramic samples at room temperature prepared by heat treatment comprising rapid heating and quenching. Temperatures in the figure refer to the target temperature of the heat treatment. (b) Composition and heat-treatment temperature dependence of the phases of Li_3PS_4 in Li_3PS_4·xLiF glass-ceramic samples. (c) F 1s XPS spectra of Li_3PS_4·xLiF glass-ceramic samples.

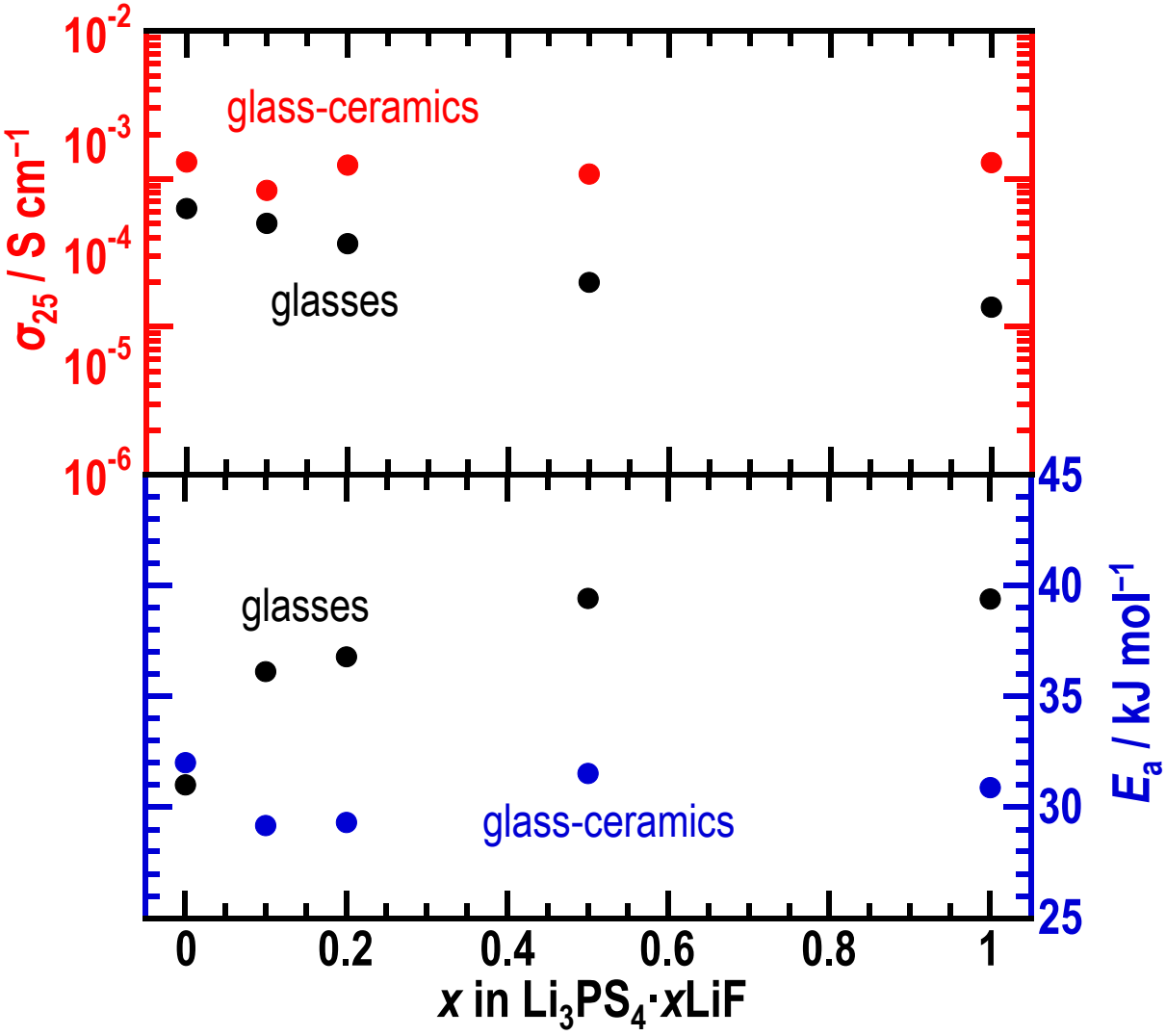

Figure 3 Ionic conductivities and activation energies of the $Li_3PS_4 \cdot xLiF$ glass and glass-ceramic samples.

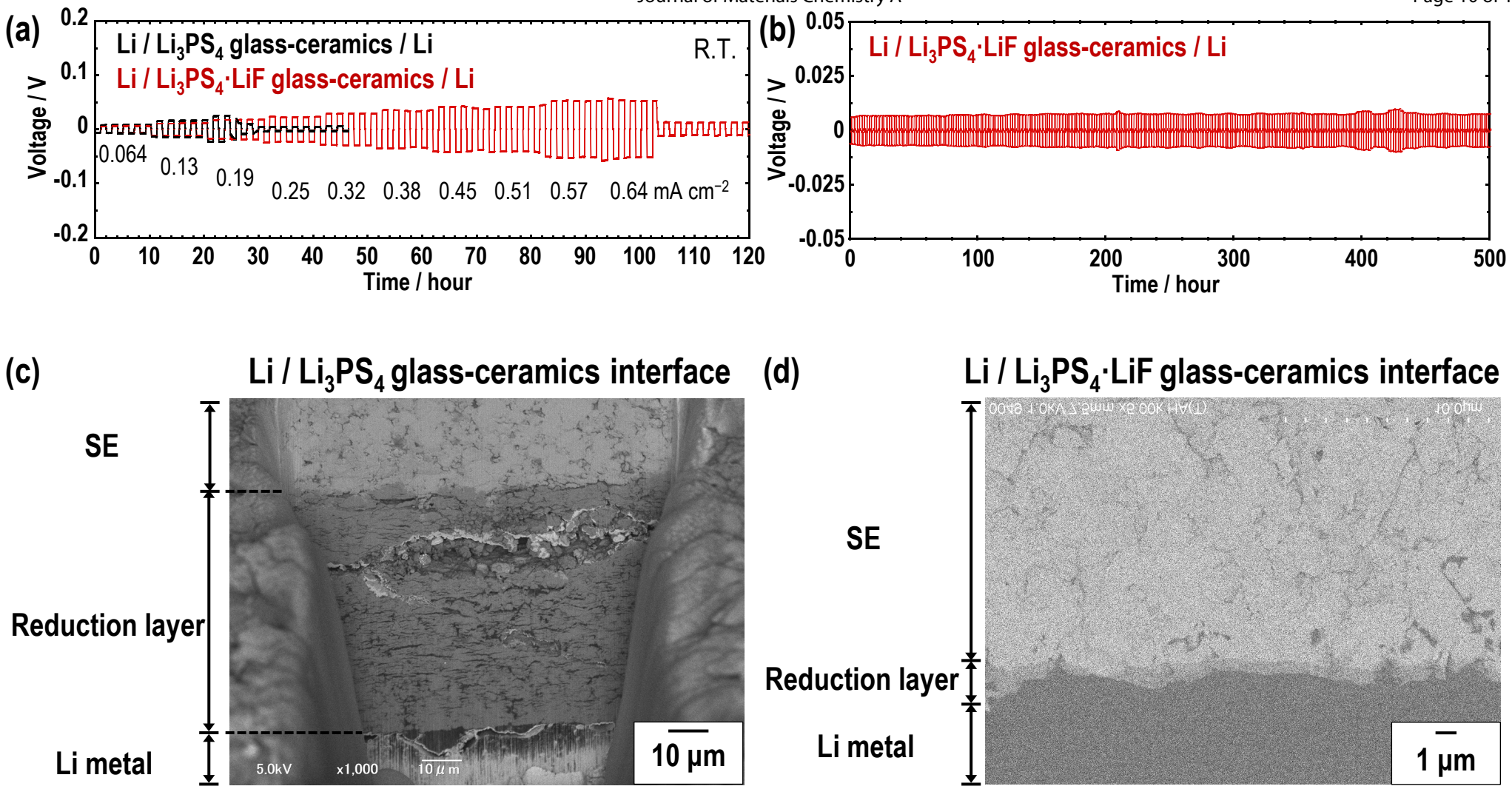

Figure 4 (a) Galvanostatic cycling tests of the Li / Li_3PS_4 or Li_3PS_4·LiF glass-ceramics / Li cells at room temperature. The applied current densities are shown in the figure. (b) Long-term galvanostatic cycling tests of Li / Li_3PS_4·LiF glass-ceramics / Li at room temperature. The applied current density was 0.1 mA cm^{-2}, and the areal capacity for half cycles was 0.1 mA h cm^{-2}. (c) Cross-sectional FIB-SEM image of the Li / Li_3PS_4 glass-ceramics interface after cycling. (d) Cross-sectional SEM image of the Li / Li_3PS_4·LiF glass-ceramics interface after cycling.

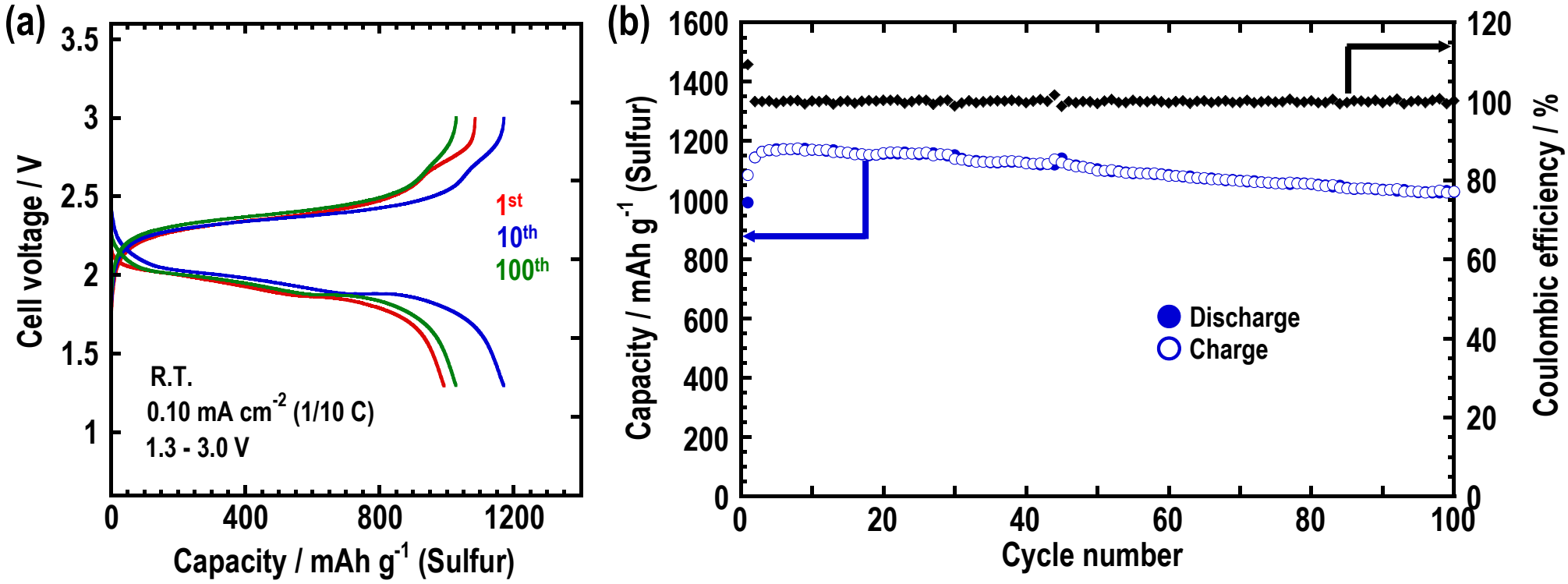

Figure 5. (a) Charge–discharge curves and (b) cycling performance of the Li/ Li_3PS_4·LiF glass-ceramics/ S–C–LPSI cell at room temperature.

Data availability statements

The data are available from the corresponding author on reasonable request.